

THE GALAXY-WEIGHTED SMALL-SCALE VELOCITY DISPERSION OF THE LAS CAMPANAS REDSHIFT SURVEY

JONATHAN E. BAKER AND MARC DAVIS

Astronomy Department, University of California, Berkeley, CA 94720

AND

HUAN LIN¹

Steward Observatory, University of Arizona, 933 N. Cherry Avenue, Tucson, AZ 85721

DRAFT October 19, 2018

ABSTRACT

The pair-weighted relative velocity dispersion of galaxies provides a measure of the thermal energy of fluctuations of the observed galaxy distribution, but the measure is difficult to interpret and is very sensitive to the existence of rare, rich clusters of galaxies. Several alternative statistical procedures have recently been suggested to relieve these problems. We apply a variant of the object-weighted statistical method of Davis, Miller, & White (1997) to the Las Campanas Redshift Survey (LCRS), which is the largest and deepest existing redshift survey that is nearly fully sampled. The derived one-dimensional dispersion on scales $\sim 1h^{-1}$ Mpc is quite low: $\sigma_1 = 126 \pm 10$ km s⁻¹, with a modest decrease at larger scales. The statistic is very stable; the six independent slices of the LCRS all yield consistent results. We apply the same statistical procedure to halos in numerical simulations of an open cosmological model and flat models with and without a cosmological constant. In contrast to the LCRS, all the models show a dispersion which increases for scales $> 1h^{-1}$ Mpc; it is uncertain whether this is a numerical artifact or a real physical effect. The standard cluster-normalized Cold Dark Matter model with $\Omega_m = 1$ as well as a tilted variant with $n = 0.8$ yield dispersions substantially hotter than the LCRS value, while models with low matter density ($\Omega_m = 0.3$) are broadly consistent with the LCRS data. Using a filtered cosmic energy equation, we measure $\Omega_m \approx 0.2$, with small-scale bias factors $b = 1.0$ – 1.5 for high-density models and $b = 0.7$ – 1.1 for low-density models.

Subject headings: cosmology — dark matter — galaxies: clustering — large-scale structure of universe

1. INTRODUCTION

The small-scale thermal energy of the observed galaxy distribution is an important diagnostic for cosmological models. For the past decade the pair velocity dispersion $\sigma_{12}(r)$ (Davis & Peebles 1983) has been the usual measure of this quantity (e.g., Bean et al. 1983; de Lapparent, Geller, & Huchra 1988; Hale-Sutton et al. 1989; Mo, Jing, & Borner 1993; Zurek et al. 1994; Fisher et al. 1994; Marzke et al. 1995; Brainerd et al. 1996; Somerville, Primack, & Nolthenius 1997; Landy, Szalay, & Broadhurst 1998; Jing, Mo, & Borner 1998). But in spite of its widespread application and the relative ease of its measurement within large redshift surveys, the $\sigma_{12}(r)$ statistic has a number of well-known deficiencies. Chief among them is its pair-wise weighting, which gives extreme influence to rare, rich clusters of galaxies containing many close pairs with high velocity dispersion.

Alternative statistics to measure the thermal energy distribution have been suggested by Kepner, Summers, & Strauss (1997) and by Davis, Miller, & White (1997, hereafter DMW). The Kepner et al. algorithm computes the pair-weighted dispersion as a function of the local galaxy density; this statistic demonstrates the heterogeneity of the environments of the local galaxy distribution, but it must be computed in volume-limited samples. The σ_1 statistic described by DMW can be estimated within a flux-limited catalog and is readily interpreted in terms of a

filtered version of the cosmic energy equation. The statistic is a measure of the rms one-dimensional velocity of galaxies, with large-scale bulk flow motions filtered out. DMW applied this statistic to the UGC catalog of optical galaxies within the Optical Redshift Survey (Santiago et al. 1995), as well as the 1.2-Jy *IRAS* catalog (Fisher et al. 1995). They showed that $\Omega_m = 1$ simulations were far too hot to match the observed dispersion. Even when compared with simulations in which the small-scale kinetic energy had been artificially lowered by a factor of four, the observed velocity distribution was colder than the simulated distribution.

However, the UGC catalog surveys a rather limited volume of the local Universe, and the *IRAS* catalog is quite dilute and under-samples dense cluster regions. It is therefore of considerable interest to apply the DMW statistic to a larger, more representative redshift survey such as the Las Campanas Redshift Survey (LCRS; Shectman et al. 1996), and to compare the results with *N*-body simulations of cosmological models which are favored by current data. This paper reports the application of this new statistic to the LCRS and compares the result to a few simulations of flat and open cosmological models. In a future paper (Baker, Davis, & Ferreira 1999), we discuss a wider variety of models, and we discuss in more detail the comparison of the LCRS with *N*-body simulations and the potential applications of σ_1 as a cosmological probe.

¹Hubble Fellow

2. APPLICATION OF σ_1 TO THE LCRS

The LCRS survey consists of 26,000 galaxies selected in a hybrid R band. The survey was conducted in six thin slices, each of size $1.5 \times 80^\circ$ on the sky, with median redshift $cz = 30,000 \text{ km s}^{-1}$. The redshift accuracy of the observations is typically $\sigma_{\text{err}} = 67 \text{ km s}^{-1}$ (Shectman et al. 1996), which is sufficient for measuring the thermal, small-scale velocity dispersion.

For measurement of σ_1 , we work with the subset of 19,306 LCRS galaxies in the range $10,000 < cz < 45,000 \text{ km s}^{-1}$, and absolute magnitude $-22.5 < M < -18.5$. To estimate the random background of the neighbors about each galaxy, we used a catalog of 268,000 randomly distributed points with the same selection function as the LCRS galaxies, including the restriction against pairs with angular separation less than $55''$ caused by limitations of optical fiber placement. Since the six slices of the LCRS are spatially separated by more than the projected separation used in the σ_1 statistic, the statistical procedure is applied to each slice individually and the results are averaged.

2.1. Method

We now briefly describe our procedure, similar to that of DMW, for determining σ_1 . For each galaxy i in a slice of the survey, we lay down a cylinder centered on the galaxy in redshift space. Let r_p be the projected radius of the cylinder and v_l its half-length along the redshift direction. For neighboring galaxies j within the cylinder, we construct the distribution $P_i(\Delta v)$, which counts the number of neighbors with redshift separation in a redshift bin centered at $\Delta v = v_j - v_i$. The counts accumulated in $P_i(\Delta v)$ are weighted by the inverse selection function ϕ_i/ϕ_j (though equal weighting yields virtually identical results). We subtract from this distribution the background distribution $B_i(\Delta v)$, which counts the number of weighted neighbors expected for an unclustered galaxy distribution. We are interested in the width of the overall distribution $D(\Delta v)$ constructed by an appropriately weighted sum over the N_g galaxies:

$$D(\Delta v) = \frac{1}{N_g} \sum_{i=1}^{N_g} w_i [P_i(\Delta v) - B_i(\Delta v)], \quad (1)$$

where the weight for galaxy i is denoted by w_i .

In order to make the statistic object-weighted rather than pair-weighted, we wish to normalize the distributions by the number of neighbors N_{ex} in excess of the random background, that is:

$$w_i^{-1} = N_{\text{ex},i} = \sum_{\Delta v} [P_i(\Delta v) - B_i(\Delta v)]. \quad (2)$$

This however presents a problem for galaxies which do not have enough neighbors to ensure that the sum is positive. DMW dealt with this problem by deleting these objects from consideration, but under half of the LCRS galaxies have at least one excess neighbor for $r_p = 1h^{-1} \text{ Mpc}$, and these galaxies are a biased sample because they populate over-dense regions. It is therefore desirable to modify the statistic to include galaxies with fewer neighbors.

We achieve a more inclusive statistic by considering separately the distributions of high- and low-density objects; that is, only galaxies with $N_{\text{ex}} \geq 1$ are included in the sum for D_{hi} , while only galaxies with $N_{\text{ex}} < 1$ are included in the sum for D_{lo} . We then weight the galaxies in the combined distribution according to

$$w_i = \begin{cases} A_{\text{hi}} N_{\text{ex},i}^{-1} & N_{\text{ex},i} \geq 1 \\ A_{\text{lo}} & N_{\text{ex},i} < 1. \end{cases} \quad (3)$$

Here A_{lo} and A_{hi} are normalization constants for the two distributions, chosen so that the distributions are weighted in proportion to the number of objects included:

$$A_{\text{hi}} = \frac{N_{\text{hi}}/N_g}{\sum_{\Delta v} [D_{\text{hi}}(\Delta v) - D_{\text{hi}}(\infty)]}, \quad (4)$$

and similarly for A_{lo} . Here N_{hi} and N_{lo} are the number of galaxies with $N_{\text{ex}} \geq 1$ and $N_{\text{ex}} < 1$, respectively, thus $N_{\text{hi}} + N_{\text{lo}} = N_g$. The baselines $D(\infty)$ are estimated from the flat tails of the distributions within 500 km s^{-1} of $\Delta v = \pm v_l$. With this normalization the final distribution obeys $\sum_{\Delta v} D(\Delta v) = 1$. Note that scaling D_{hi} and D_{lo} by the constants A does not affect the derived widths for these distributions; rather, it merely alters the weighting of the two in the combined distribution.

This procedure, in contrast to that of DMW, allows us to include all of the available data, yielding an unbiased, object-weighted measure of the thermal energy of the galaxy distribution. It is the object-weighting which differentiates our procedure from the more traditional measure of the pair dispersion $\sigma_{12}(r)$; all galaxies (not pairs) are assigned equal weight in our statistic σ_1 .

We measure the width of the distribution $D(\Delta v)$ using the convolution procedure outlined by DMW (equation 18), in which a velocity broadening function $f(v)$ is convolved with the two-point correlation function $\xi(r)$ to produce a model $M(\Delta v) = \bar{\xi}_{r_p} * f$ for $D(\Delta v)$:

$$M(\Delta v) = \int_0^{r_p} dr 2\pi r \int_{-\infty}^{\infty} dy \xi(\sqrt{r^2 + y^2}) f(\Delta v - y). \quad (5)$$

The two-point correlation function of the LCRS is well-approximated by $\xi(r) = (r_0/r)^\gamma$, with $r_0 = 5h^{-1} \text{ Mpc}$ and $\gamma = 1.8$ (Jing et al. 1998), while for the N -body simulations we use the cylindrically averaged mass correlation function $\bar{\xi}_{r_p}(\Delta v)$ measured directly from the particle distribution. We find that an exponential broadening function (see Diaferio & Geller 1996; Sheth 1996, Juszkiewicz, Fisher, & Szapudi 1998)

$$f(v) = \frac{1}{\sigma_1} \exp\left(-\frac{|v|}{\sigma_1}\right) \quad (6)$$

provides a much better fit to the LCRS data and all N -body models than does a Gaussian. Here we have defined the width σ_1 so that it is a measure of the rms velocity of individual galaxies in one dimension (with bulk motions on scales $\gtrsim 1h^{-1} \text{ Mpc}$ filtered out). The (object-weighted) rms difference in velocity between any two galaxies is then $\sigma_1\sqrt{2}$ (DMW call this quantity, which is equal to the rms dispersion of the distribution f , the ‘‘intrinsic’’ dispersion σ_I ; we will work exclusively with σ_1 to avoid confusion).

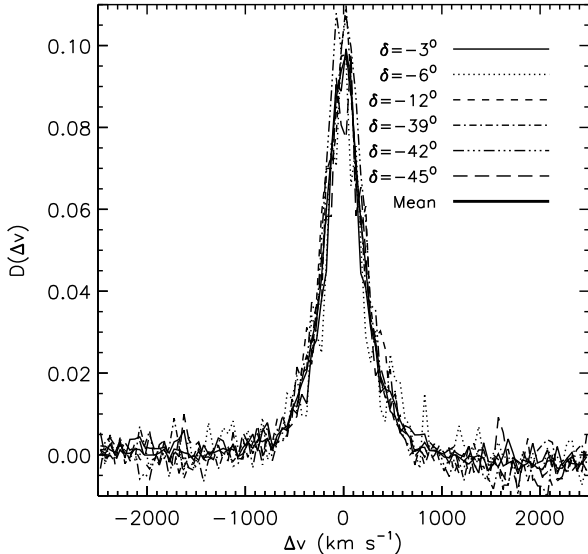


FIG 1.— Galaxy-weighted velocity distribution $D(\Delta v)$ for the six LCRS slices.

The three-dimensional dispersions are larger by an additional factor $\sqrt{3}$.

We perform a nonlinear χ^2 -minimization fit to determine the width σ_1 and amplitude of the model $M(\Delta v)$. Before fitting, we convolve the model with a Gaussian of rms $\sigma_{\text{err}}\sqrt{2} = 95 \text{ km s}^{-1}$ to account for the LCRS redshift measurement uncertainties; the factor of $\sqrt{2}$ converts from the measurement uncertainty for individual redshifts to the uncertainty for redshift differences, which are accumulated in $D(\Delta v)$. We also include baseline terms in the model which are constant and linear in Δv , for a total of four fit parameters. The linear term is necessary for the LCRS because for simplicity we define “cylinders” in redshift space based on projected angular separation on the sky. This leads to a small gradient in the measured distribution function $D(\Delta v)$ because the “cylinders” are in fact conic sections, but the term is quite small because the length of the cylinders, $2v_l$, is much smaller than the typical redshift of galaxies in the survey. Although the gradient term has a negligible effect on the derived width, it does improve significantly the quality of the χ^2 fit.

2.2. Results for the LCRS

We have used the six independent slices of the LCRS to estimate the errors in $D(\Delta v)$ as a function of Δv in computing χ^2 . However, we expect that the bins may be correlated due to sample variance; the fitting procedure is therefore not strictly legitimate, but the consistency of the results for the widths of the individual slices serves as a check on the degree to which sample variance affects the result. We also expect $\chi^2_\nu > 1$ if the exponential broadening function of width σ_1 (assumed independent of r) provides an inadequate description of the small-scale velocities.

The $D(\Delta v)$ distributions for the six independent LCRS slices are plotted in Figure 1, and Table 1 lists the derived widths. The second to last line gives the mean and standard deviation of the mean for separate fits to the six slices, while the last line is the result of a single fit to the combined distribution of all galaxies. Note that

the dispersion measured for objects with excess neighbors ($N_{\text{ex}} \geq 1$) is clearly higher than that measured for objects with fewer neighbors. This behavior is expected because objects with more neighbors are found in regions of higher density, which tend to be hotter.

The fit to the LCRS $D(\Delta v)$, shown in Figure 2, is quite good, with $\chi^2_\nu = 117/96 = 1.22$; the probability of χ^2 exceeding this value is $1 - P(\chi^2|\nu) = 7\%$. The best-fitting Gaussian $f(v)$ is much worse, with $\chi^2_\nu = 1.84$ and $1 - P(\chi^2|\nu) = 10^{-6}$.

Based on the mean of the six slices we adopt $\sigma_1 = 126 \pm 10 \text{ km s}^{-1}$. This value has been computed for $r_p = 1h^{-1} \text{ Mpc}$ and $v_l = 2500 \text{ km s}^{-1}$. The results are quite insensitive to cylinder length, ranging only from $117 \pm 14 \text{ km s}^{-1}$ at $v_l = 1500 \text{ km s}^{-1}$ to $132 \pm 13 \text{ km s}^{-1}$ at $v_l = 3500 \text{ km s}^{-1}$. Our chosen value $v_l = 2500 \text{ km s}^{-1}$ is large enough to allow a clean measure of the tails of the distribution without significant non-linearities in the baseline gradient due to variations in the selection function.

A modest decrease in σ_1 is evident as r_p is increased above $r_p = 1h^{-1} \text{ Mpc}$ (see Table 2). Although the $D(\Delta v)$ distributions are very insensitive to r_p , the averaged correlation function $\bar{\xi}_{r_p}(\Delta v)$ becomes broader as r_p increases. As a result, smaller values of r_p provide a cleaner measure of the true (real-space) velocity broadening on small scales, but decreasing r_p below $1h^{-1} \text{ Mpc}$ reduces the signal-to-noise, as most galaxies have too few neighbors. The background subtraction also becomes cleaner as r_p is reduced.

Note that for the larger value $r_p = 2h^{-1} \text{ Mpc}$ used

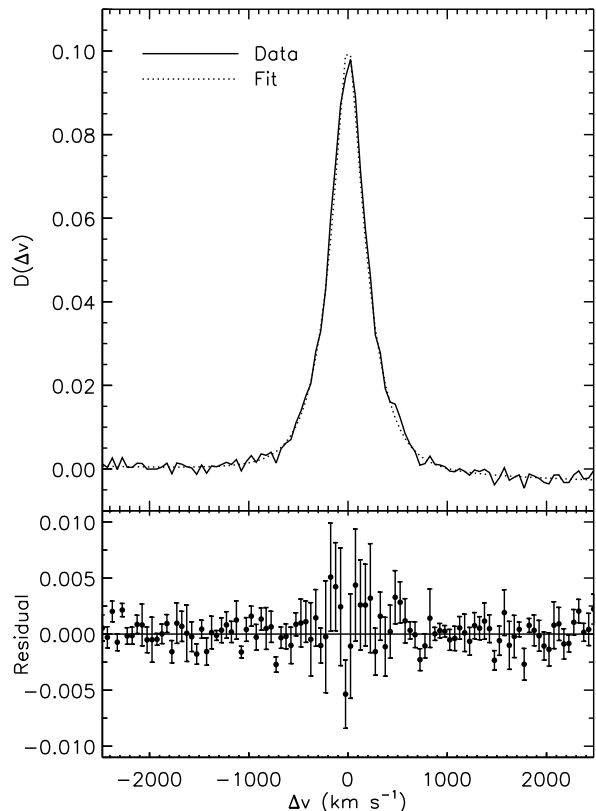


FIG 2.— Velocity distribution $D(\Delta v)$ and fit for the combined LCRS data (upper panel), and residuals for the fit with errors estimated from the standard deviation of the six slices (lower panel; note the change in vertical scale).

Slice	Dec.	σ_1 (km s ⁻¹)			N_{hi}/N_g	N_g
		All	$N_{\text{ex}} \geq 1$	$N_{\text{ex}} < 1$		
1	-3°	96	184	53	0.44	3540
2	-6°	103	255	73	0.34	2067
3	-12°	163	273	129	0.44	3754
4	-39°	117	181	94	0.41	3265
5	-42°	136	178	112	0.44	3503
6	-45°	142	171	131	0.43	3177
Mean		126 ± 10	207 ± 18	99 ± 13	0.42	3218
1-6		136	208	101	0.42	19306

TABLE 1

The σ_1 statistic for the six LCRS slices. The second to last line gives the mean and standard deviation of the mean of the independent slices, while the last line is the result of a fit to the entire dataset. We list σ_1 for the combined dataset and for the subsets of galaxies with $N_{\text{ex}} \geq 1$ and $N_{\text{ex}} < 1$. N_{hi}/N_g is the fraction of galaxies with $N_{\text{ex}} \geq 1$, and N_g is the total number of galaxies.

by DMW, our result is $\sigma_1 = 114 \pm 10$ km s⁻¹. If, as in the DMW analysis, we do not account for broadening due to redshift measurement errors, the result increases to $\sigma_1 = 136 \pm 9$ km s⁻¹. Since the two surveys have comparable redshift uncertainties, our LCRS result is perfectly consistent with the value $\sigma_1 = 130 \pm 15$ km s⁻¹ which DMW derived for the much smaller UGC catalog.

3. COMPARISON TO *N*-BODY MODELS

We have completed a suite of *N*-body simulations designed to predict the small-scale velocity dispersion in a variety of cosmological models. Here we discuss the results of a few of these models: the “standard” Cold Dark Matter (SCDM) model and a tilted variant (TCDM), a model with a cosmological constant Λ (LCDM), and an open model (OCDM). The cosmological parameters for these models are listed in Table 3. All models are approximately normalized to the present-day abundance of clusters; the LCDM and TCDM models additionally satisfy the *COBE* normalization. The SCDM model is known to fail a number of cosmological tests and is included for historical reasons, and only LCDM is fully consistent with current limits from high-redshift supernovae (Perlmutter et al. 1999). We note that on the scales relevant for our simulations, the TCDM power spectrum is indistinguishable from a τ CDM spectrum with shape parameter $\Gamma = 0.2$. A broader range of models and a more detailed discussion of the simulations may be found elsewhere (Baker et al. 1999).

Initial power spectra were obtained using the CMBFAST code (Seljak & Zaldarriaga 1996, 1998). The simulations were evolved on a 128³ mesh using a P³M code

(Briau, Summers, & Ostriker 1995) in which short-range forces are computed using a special purpose GRAPE-3AF board (Okumura et al. 1993). We chose a box of size $L = 50h^{-1}$ Mpc to match the length of the LCRS cylinders; with $N_p = 64^3$ particles this gives a mass resolution of $1.3 \times 10^{11} \Omega_m h^{-1} M_\odot$, where $h = H_0/100$ km s⁻¹ Mpc⁻¹. A Plummer force softening $\epsilon = 50h^{-1}$ kpc was used. The simulations were started at redshifts $z_i = 15$ (for $\Omega_m = 1$) or $z_i = 19$ (for $\Omega_m = 0.3$) and evolved to $z = 0$ in 1500 time-steps using $p = a^2$ as the integration variable.

The simulations are converted to “redshift” space by adding the velocities v_i along one of the three coordinates i to the positions x_i : $x_i \rightarrow x_i + v_i/H$, where H is the Hubble constant. Periodic boundary conditions are applied at the box edges. We then apply exactly the same statistical procedure for determining σ_1 as for the LCRS, except that the selection function is now unity.

3.1. Tests of σ_1 Measurements

We have used our *N*-body simulations to perform a number of checks on the robustness of our method for determining the small-scale velocity dispersion. One test is to ask how well our model is able to account for the redshift measurement uncertainties in the LCRS. To simulate these uncertainties, we added Gaussian random velocities of rms σ_{err} along the “redshift” coordinate in the simulations. We then make two determinations of σ_1 , which should ideally be equal. In one determination, the random velocities have been added and we perform an extra Gaussian convolution in the model to account for them. In the other, no random velocities are added and no Gaus-

r_p (h^{-1} Mpc)	σ_1 (km s ⁻¹)	N_{hi}/N_g
0.5	136 ± 10	0.23
1	126 ± 10	0.42
1.5	107 ± 8	0.55
2	96 ± 12	0.63
2.5	99 ± 13	0.68

TABLE 2

LCRS dispersion σ_1 as a function of limiting projected radius r_p , and fraction of galaxies with excess neighbors.

Model	Ω_m	Ω_Λ	n	h	σ_8
SCDM	1	0	1	0.5	0.7
TCDM	1	0	0.8	0.5	0.7
LCDM	0.3	0.7	1	0.7	1
OCDM	0.3	0	1	0.7	1

TABLE 3

Cosmological parameters for N -body models: matter density Ω_m , cosmological constant Ω_Λ , tilt n where $P(k) \propto k^n$, Hubble constant $H_0 = h/100 \text{ km s}^{-1} \text{ Mpc}^{-1}$, and rms mass fluctuation σ_8 in spheres of radius $8h^{-1} \text{ Mpc}$.

sian convolution is necessary. We find that the two widths agree quite well, to within 10 km s^{-1} over the range of interest for σ_1 ($100\text{--}300 \text{ km s}^{-1}$). The agreement improves as σ_1 increases and the uncertainties contribute relatively less to the width of the observed velocity distribution.

A second test of the method is to compare velocity widths measured in real space with those measured in cylinders in redshift space. For this test, we replace the velocities of the simulation particles with velocities drawn from a random exponential distribution of a given rms σ . It is straightforward to show that the velocity distribution appropriate for the difference distribution $D(\Delta v)$ is then

$$f(v) = \frac{1}{2\sigma^2} \left(|v| + \frac{\sigma}{\sqrt{2}} \right) \exp \left(-\sqrt{2} \frac{|v|}{\sigma} \right). \quad (7)$$

Using this form in the redshift-space model (Equation 5), we find that our procedure recovers the true velocity dispersion with an accuracy better than 10% for σ_1 in the range $100\text{--}300 \text{ km s}^{-1}$.

Finally, we can test the extent to which our measurement of σ_1 in the long redshift-space cylinders is contaminated by motions on scales larger than $1h^{-1} \text{ Mpc}$. First we construct distributions analogous to $D(\Delta v)$, but measured in real space, with neighbors drawn from spheres of radius $1h^{-1} \text{ Mpc}$ in the simulations. These are compared to distributions with neighbors drawn from the long cylinders, also measured in real space. The widths of these distributions agree to within 1%, and we conclude that the contamination from large scales is negligible.

3.2. Selection of Galaxies from the Mass Distribution

We can easily compute σ_1 for particles in the simulations, but the observed small-scale dispersion of galaxies, which correspond in some way to halos in the simulations, will in general differ from that of the mass. The internal velocity dispersions of galaxies are not included in the observed statistic; moreover, the galaxy population may be a biased tracer. In order to test whether our simulations can

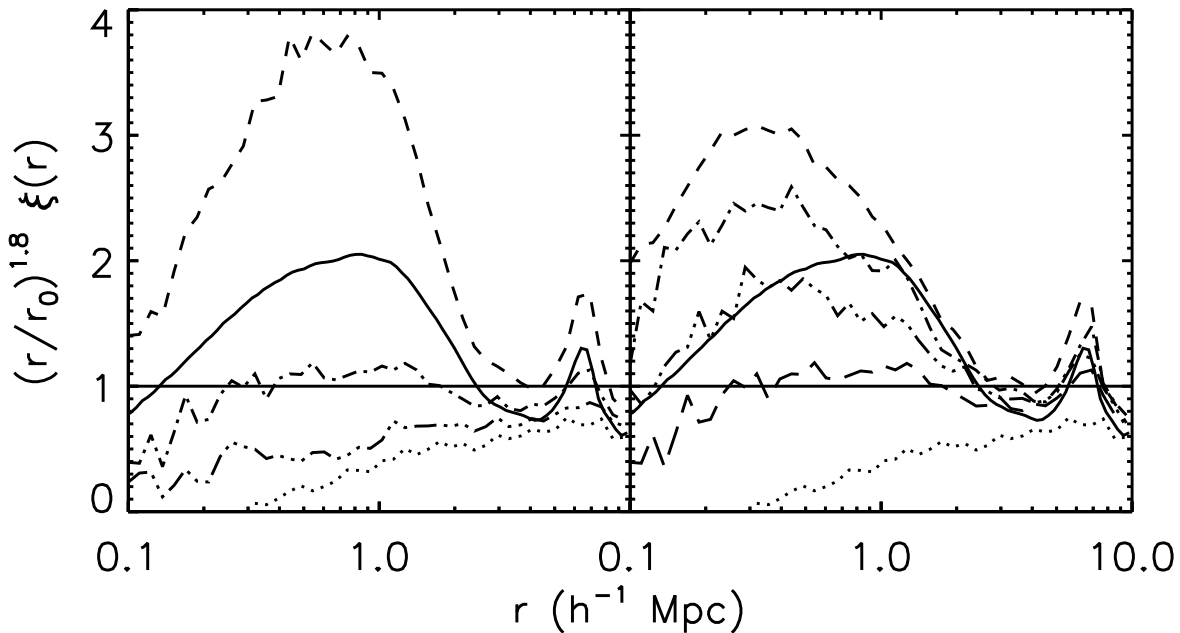


FIG. 3.— Two-point correlation functions multiplied by $(r/r_0)^{1.8}$ for LCDM simulation halos for a range of N_s and α . Here $r_0 = 5.1h^{-1} \text{ Mpc}$ and the LCRS $\xi(r)$ appears as a solid horizontal line. In both plots, the curve at bottom (dotted line) shows $N_s = \infty$ (no halo splitting), and the solid curve shows the mass correlation function. In the plot at left, N_s is held fixed at 80, while α takes on the values 0, 0.25, 0.5 (top to bottom). In the plot at right, α is held fixed at 0.25, while N_s takes on the values 10, 20, 40, 80 (top to bottom).

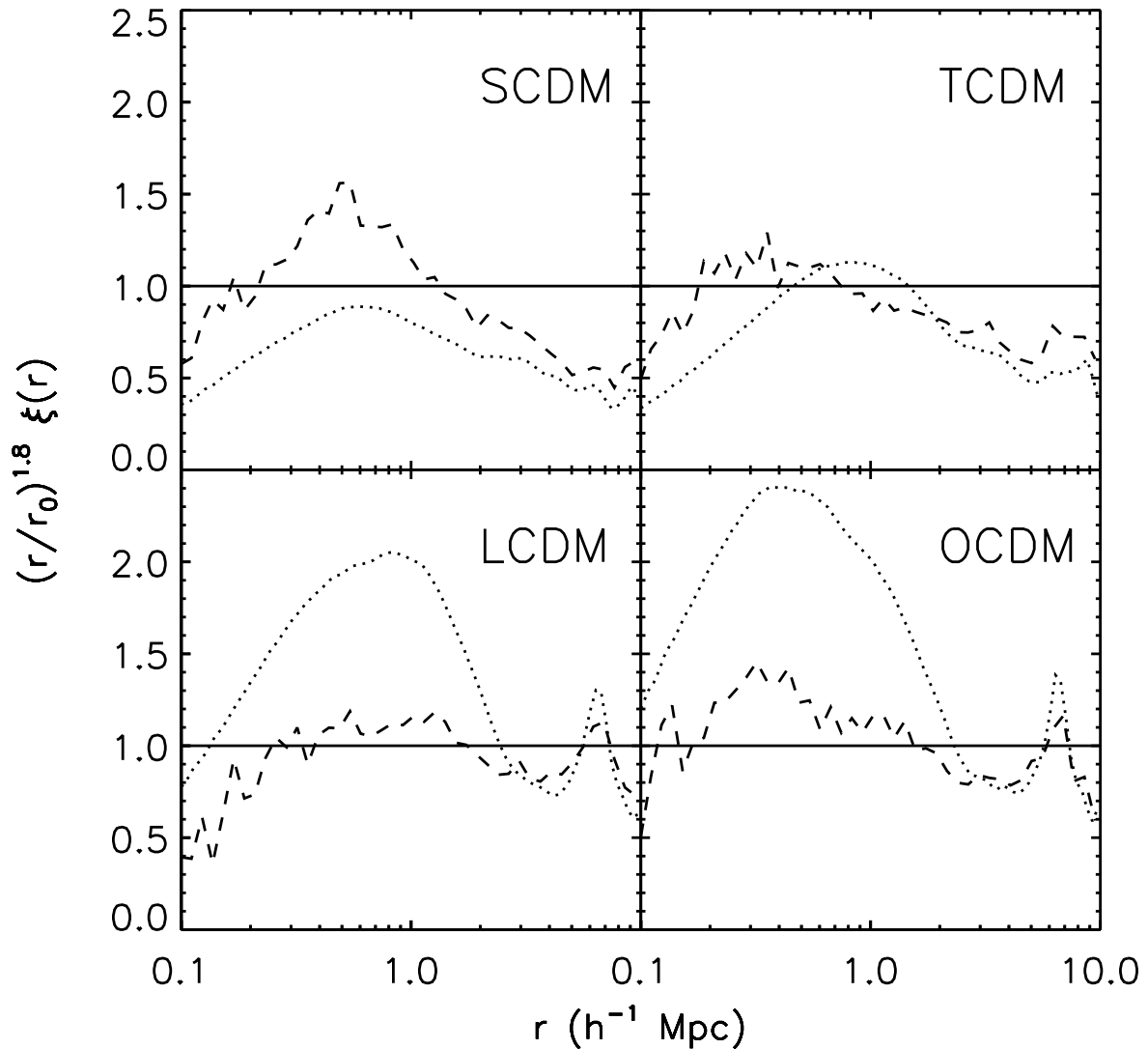


FIG. 4.— Two-point correlation functions for the mass (dotted lines), halos (dashed), and LCRS (solid), plotted as in Fig. 3. Halos were selected using the parameters listed in Table 4.

reproduce the LCRS result for σ_1 , it is therefore important to identify “galaxies” within the N -body simulations. Unfortunately the process of galaxy formation includes baryonic physics on a wide range of scales not probed by our dark-matter only simulations. For the present work, we define galaxies using a simple phenomenological model which we expect to yield similar results to those of larger gas-dynamical simulations.

We first apply the standard friends-of-friends (FOF; Davis et al. 1985) algorithm to the simulations, with a linking length of 0.2 mesh cells and a minimum group size $N \geq 10$, corresponding to halos with mass $M \gtrsim 10^{12} \Omega_m h^{-1} M_\odot$. We have also considered the HOP method (Eisenstein & Hut 1998) for defining halos, but we obtain similar results for reasonable parameter choices and do not discuss them here.

Our limited resolution and the nature of the FOF al-

gorithm lead to a serious and well-known over-merging problem, in which a large cluster containing many galaxies will be identified as a single halo. This drastically lowers the small-scale velocity dispersion because the motions of galaxies within clusters are neglected. To remedy this situation, we split halos with more than N_s particles by randomly selecting particles from within the halos and identifying these particles as galaxies. Halos identified in this way will again include the internal motions of galaxies, but as the splitting is only applied to large, hot halos ($N_s \gg 10$), we expect these internal motions to have a negligible effect on our result. Small halos with fewer than N_s particles are taken to be individual galaxies.

For comparison with the LCRS, we wish to choose a set of halos which resemble the LCRS galaxies as closely as possible. Some N -body models yield a correlation function $\xi(r)$ which is too steep, and it is therefore advantageous

Model	N_s	α	N_{halos}	σ_1 (km s $^{-1}$)	
				Mass	Halos
SCDM	80	0.00	2624	310	269
TCDM	40	0.25	2351	320	293
LCDM	80	0.25	1901	188	143
OCDM	80	0.20	2128	197	158

TABLE 4

Velocity width σ_1 for the N -body simulations. Results are listed for all particles and for the N_{halos} halos identified using our splitting procedure with parameters N_s and α .

to select halos which are anti-biased on small scales (Jing et al. 1998). We accomplish this through our halo-splitting procedure by drawing random particles with a probability p which has a power-law dependence on the number of particles N in the parent halo: $p(N) = N_s^{\alpha-1} N^{-\alpha}$, with $\alpha > 0$. The number of galaxies per unit halo mass then falls as $N^{-\alpha}$ for large halos. We choose parameters N_s and α which simultaneously mimic the power-law shape of the LCRS correlation function and produce approximately the correct number density of galaxies, $n \approx 0.02h^3 \text{ Mpc}^{-3}$, implying 2500 galaxies per simulation volume. Increasing α tends to flatten the correlation function on small scales and yields fewer halos; increasing N_s at fixed α tends to lower the correlation amplitude and also yields fewer halos. This behavior is illustrated in Figure 3 for the LCDM model.

Figure 4 shows the correlation functions for our selected halos in each of the models. In the low-density models, we are able to select halos which match the LCRS $\xi(r)$ quite well. The normalization of the high-density models is such that $\xi(r)$ always falls below the LCRS power law on large scales. The TCDM halos match well at $r \lesssim 2h^{-1} \text{ Mpc}$. In the SCDM model, we are unable to reproduce exactly the shape of $\xi(r)$ without falling too far below the LCRS amplitude and producing too few halos. However, the differences in J_2 (see §3.4) computed from these correlation functions show that this mismatch should affect our estimate of Ω_m by at most 30%.

3.3. Results for σ_1

The results for σ_1 for our four cosmological models are listed in Table 4. We see that the mass in the two $\Omega_m = 1$ models is far too hot on $1h^{-1} \text{ Mpc}$ scales, with σ_1 well over twice the LCRS value. The spectral tilt of the TCDM model has very little effect on the small-scale velocities, as the result is nearly identical to the SCDM result. The mass in the low- Ω_m models, on the other hand, is also hotter than the LCRS, but only by a factor of about 1.5.

The halos in the simulations are somewhat cooler than the mass, with small-scale dispersions lower by factors in the range 0.7–0.9. The LCDM halos come closest to the LCRS value; at 143 km s^{-1} , they are only marginally (1.7σ) hotter than the LCRS. The open model produces velocity dispersions slightly higher than the LCDM model, while the halos in the $\Omega_m = 1$ models are again much hotter than the LCRS data.

Figure 5 shows that the exponential $f(v)$ provides an excellent fit to the velocity distributions measured in the simulations in redshift space. We show distributions for the N -body mass particles and for the halos. The halo

distributions are noisier because there are many fewer halos than mass particles in the simulation volumes. The distributions for the SCDM and OCDM models are nearly indistinguishable from the TCDM and LCDM distributions, respectively, and are not shown.

We have also computed σ_1 for galaxies drawn using more sophisticated semi-analytic techniques from a large Virgo simulation (Benson et al. 1999) of the LCDM model. This simulation has a mass resolution better than ours by about a factor of two, and the box length is nearly three times as large. The result is 126 km s^{-1} , only slightly lower than our value of 143 km s^{-1} . This suggests that our procedure for defining galaxies is reasonable. The Virgo result exactly matches the LCRS dispersion, which suggests that the small-scale velocity dispersion predicted by the $\Omega_m = 0.3$ flat model is in fact perfectly consistent with the observational data. Further details of this comparison will be presented in a future work (Baker et al. 1999).

As noted in §2.2, the LCRS velocity width decreases somewhat as the limiting radius $r_{p,\text{max}}$ is increased. In Figure 6, we show this scale dependence measured in independent cylindrical shells of width $1h^{-1} \text{ Mpc}$, where the limits on the radial integration in the model (Equation 5) have been adjusted appropriately. Although the measured LCRS $D(\Delta v)$ shows little scale dependence, the integrated correlation function broadens with scale, leading to a smaller measured velocity width.

None of the N -body models, however, are able to reproduce the scale dependence observed in the LCRS. The halos drawn from the Virgo simulation, which show very little scale dependence, come closest, while the other models tend to show an increase in velocity dispersion with scale. Only the LCDM model is shown in Figure 6, but we find similar discrepancies for the other models as well. Although the $\Omega_m = 0.3$ LCDM model produces a reasonable match to the velocity dispersion on very small scales, all of the models seem unable to reproduce the observed coldness of the velocities on intermediate scales $\sim 1\text{--}3h^{-1} \text{ Mpc}$. At present it is unclear whether this discrepancy is due to problems with the galaxy selection procedure, the resolution of the simulations, or a more fundamental flaw in the cosmological models.

3.4. Filtered Cosmic Energy Equation

The σ_1 statistic is ideally suited for the application of the cosmic energy (Layzer-Irvine) equation filtered on small scales. As shown by DMW, we expect $\sigma_1^2 \propto \Omega_m J_{2,m}$ in

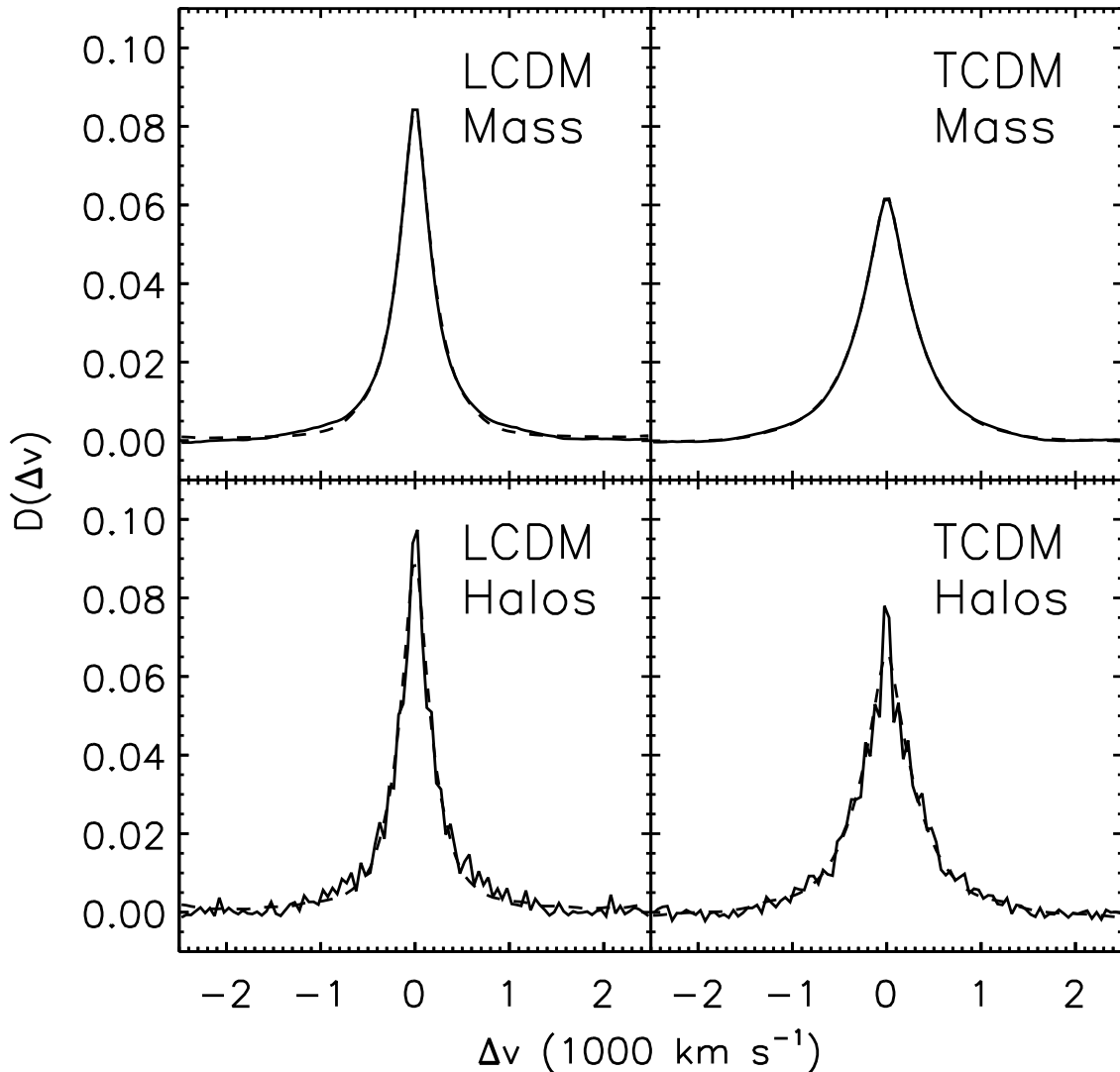


FIG. 5.— Velocity distributions (solid) and fits (dashed) for two representative N -body models. In each plot the fit is shown as a dashed line and is generally invisible because it is obscured by the measured distribution. Top and bottom panels show the distributions for all particles and for halos, respectively.

the absence of velocity bias, where

$$J_2 = \int_{r_{\min}}^{r_{\max}} dr r \xi(r). \quad (8)$$

The subscript m means that J_2 is computed from $\xi_m(r)$, the correlation function for the underlying mass. We can write this in terms of the measured $\xi(r)$ of an observed sample j by defining an effective bias $b_j^2 = J_{2,j}/J_{2,m}$. If we then compare $\sigma_{1,j}$ measured for sample j with $\sigma_{1,N}$ measured for the underlying mass in an N -body simulation with mass density parameter Ω_N , we can measure the parameter

$$\Omega_m/b_j^2 = \left(\frac{\sigma_{1,j}}{\sigma_{1,N}} \right)^2 \left(\frac{J_{2,N}}{J_{2,j}} \right) \Omega_N. \quad (9)$$

If in addition we can choose a sample of N -body halos which matches the correlation function of the sample j , then we have a direct measure of Ω_m :

$$\Omega_m = (\sigma_{1,j}/\sigma_{1,N})^2 \Omega_N, \quad (10)$$

where $\sigma_{1,N}$ is now measured for the N -body halos rather than the underlying mass.

The results of combining the LCRS dispersion $\sigma_1 = 126 \pm 10 \text{ km s}^{-1}$ with our four cosmological N -body models are listed in Table 5. Based on the halos in each of the four simulations, we derive consistent values $\Omega_m \approx 0.2$. Note that the errors listed on Ω_m are $1\text{-}\sigma$ uncertainties derived solely from the LCRS σ_1 result; they do not include any systematic errors in the model results. The fact that we derive similar values of Ω_m from each of the different models is an important consistency check, and gives us

Model	Ω_m	Ω_m/b^2	b
SCDM	0.22 ± 0.03	0.10–0.14	1.2–1.5
TCDM	0.18 ± 0.03	0.12–0.15	1.0–1.3
LCDM	0.23 ± 0.04	0.20–0.27	0.8–1.1
OCDM	0.19 ± 0.03	0.20–0.29	0.7–1.0

TABLE 5

Density parameter and small-scale bias derived from the cosmic energy equation and the LCRS dispersion.

confidence that our method is indeed a sensitive probe of the matter density.

Table 5 also lists the values of Ω_m/b^2 derived by comparing the LCRS dispersion with the dispersion of the N -body mass. The integral J_2 converges rather slowly, and its value is quite sensitive to the integration limits r_{\min} and r_{\max} . A reasonable lower limit is $r_{\min} = 0.1 h^{-1}$ Mpc, which eliminates from the analysis the internal velocity dispersion of typical galaxies and includes only the dispersion of galaxies moving relative to each other. We might also take r_{\max} to be slightly larger than $1 h^{-1}$ Mpc, since the length of the redshift-space cylinders means that there will be some contribution to σ_1 from larger scales (although we have measured this effect in the simulations and have found that it is very small). The ranges shown for Ω_m/b^2 were obtained by allowing r_{\min} and r_{\max} to vary over the ranges 0.05–0.2 and 1–5 h^{-1} Mpc, respectively. Our results for the high-density models are consistent with the value $\Omega_m/b^2 = 0.14 \pm 0.05$ found by DMW, who only considered an $\Omega_m = 1$ model.

The parameter Ω_m/b^2 is approximately equal to β^2 , where $\beta \approx \Omega_m^{0.6}/b$ is the parameter measured by large-scale flow analyses. We find $\beta \approx 0.3$ –0.4 for the two high-density models, and $\beta \approx 0.45$ –0.55 for the two low-density models. These ranges are generally consistent with some large-scale flow determinations (e.g., Willick & Strauss 1998; Baker et al. 1998; Davis, Nusser, & Willick 1996) but not with the POTENT analyses, which prefer $\beta \sim 1$ (e.g., Sigad et al. 1998). Of course, the bias may in general depend on scale, in which case our small-scale result need not match the β values measured using flows on much larger scales.

Finally, we can combine the values of Ω_m and Ω_m/b^2 to obtain an estimate of the bias of the galaxy distribution on small scales. Our high-density models require biases $b = 1.0$ –1.5, while the low-density models are slightly anti-biased, $b = 0.7$ –1.1. These ranges are consistent with the biases measured directly from the correlation functions of the simulations.

3.5. Effects of Streaming Velocities

Although our goal is to measure the particle distribution function from redshift-space information alone, we must do this by considering the relative motions of pairs of galaxies, for which we expect mean streaming as well as thermal motions. As defined in Equation 6, our model does not account for a non-zero first moment of the velocity distribution of pairs of galaxies. However, the first moment will, in general, be non-negligible due to the mean tendency of galaxies to approach each other, and it will contaminate a measurement of the second moment. On small scales in virialized clusters, for example, the infall velocity approximately cancels the Hubble expansion, and so its presence

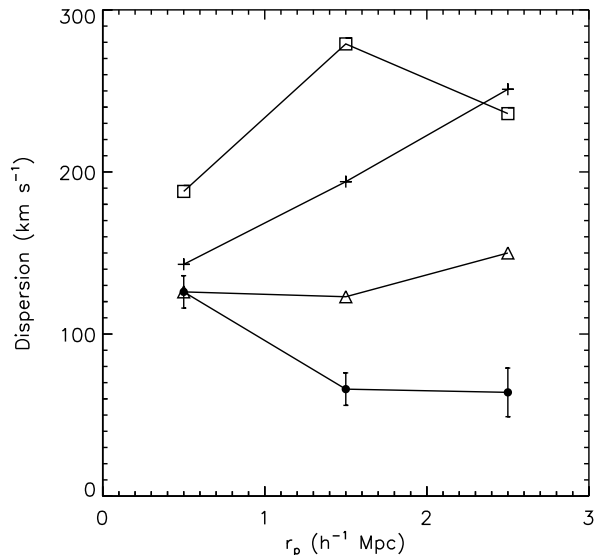


FIG 6.— Object-weighted velocity dispersion measured in independent cylindrical shells of width $1 h^{-1}$ Mpc. The LCRS data are shown as filled circles with error bars. Also shown are LCDM mass (squares) and halos drawn from our simulations (crosses) and from the Virgo simulation (triangles).

can affect our measurements on $1 h^{-1}$ Mpc scales by of order 100 km s^{-1} . Jing & Boerner (1998) have shown that the effect of the streaming motions on the estimate of the pairwise velocity dispersion can be dramatic, increasing σ_{12} from $\sim 400 \text{ km s}^{-1}$ to 580 km s^{-1} at $1 h^{-1}$ Mpc separation.

The effects of the streaming motions can be incorporated into our analysis by writing the distribution function in Equation 5 as

$$f(v) = -\frac{1}{\sigma'_1} \exp\left(-\frac{|v - \bar{v}_1|}{\sigma'_1}\right), \quad (11)$$

where \bar{v}_1 is the mean object-weighted streaming velocity, which is a function of separation, and σ'_1 is the second moment of the streaming-corrected velocity distribution. The form of \bar{v}_1 is unknown but can be measured directly from N -body simulations.

Our estimate of σ_1 with $\bar{v}_1 = 0$ will be smaller than σ'_1 because streaming motions tend to cause objects to pile up at small velocity separations in redshift space. However, σ_1 has the advantage that it is a model-independent statistic, relying only on the assumption of an exponential velocity distribution. The comparison of the data with N -body models is also consistent; to the extent that the

F	$\sigma'_{1,\text{LCRS}}$	χ^2_ν	$\sigma'_{1,\text{LCDM}}$
0	126 ± 10	1.22	143
0.5	162 ± 12	1.20	195
1	201 ± 13	1.25	245
1.5	239 ± 14	1.35	292

TABLE 6

Velocity widths with corrections for self-similar streaming motions applied. Results are listed for the LCRS and for halos drawn from our LCDM simulation.

models describe the real universe, the same streaming motions will be present in both the data and the models, and will affect the estimates of σ_1 similarly. Incorporating a non-zero \bar{v}_1 introduces model dependencies into the measurement, and there is no guarantee that the infall measured in the N -body simulations matches that of the real universe.

For the application of the cosmic energy equation, it is in fact more appropriate to use σ_1 rather than σ'_1 , because contributions from both random thermal motions and mean streaming motions are already included. On the other hand, σ'_1 is a better measure of the truly thermal energy of the galaxy distribution. We can estimate it by using Equation 11 with an appropriate model for \bar{v}_1 . For the mean pairwise velocity, the simple form

$$\bar{v}_{12}(r) = -\frac{FH_0r}{1 + (r/r_0)^2}, \quad (12)$$

(Davis & Peebles 1983) is often used, where F is a numerical factor, typically $F = 1$ – 1.5 . Another expression has been proposed more recently by Juszkiewicz, Springel, & Durrer (1999):

$$\bar{v}_{12}(r) = -\frac{2}{3}fH_0r\bar{\xi}(r) \left[1 + \alpha\bar{\xi}(r)\right], \quad (13)$$

where $f \approx \Omega_m^{0.6}$, $\alpha \approx 1.2 - 0.65\gamma_0$ with $\gamma_0 \equiv -d \ln \xi / d \ln r|_{\xi=1}$, and

$$[1 + \xi(r)]\bar{\xi}(r) = \frac{3}{r^3} \int_0^r dx x^2 \xi(x). \quad (14)$$

These two forms for $\bar{v}_{12}(r)$ are nearly equal at small scales $r \lesssim 10h^{-1}$ Mpc if we set $F = 1.8\Omega_m^{0.6}$; note that $F = 1$ corresponds to streaming motions which just cancel the Hubble expansion on small scales.

Table 6 shows that the streaming correction has a substantial effect on the derived LCRS velocity width, with σ'_1 rising to 201 ± 13 km s $^{-1}$ for $F = 1$ and 261 ± 15 km s $^{-1}$ for $F = 1.8$. The χ^2 statistic worsens somewhat for $F > 1$. The N -body models show similar behavior. We caution, however, that the streaming-corrected dispersions are model-dependent and are not an appropriate measure of the single-particle dispersion for use with the cosmic energy equation, which is defined in the comoving frame of the universe. This is in contrast to analyses of the pair dispersion, where it is appropriate to use the cosmic virial theorem, defined in the mean streaming frame.

4. CONCLUSIONS

Although the potential of small-scale cosmological velocities as a cosmological probe has long been recognized, the application of pair-weighted statistics is problematic. We apply an extended version of the more stable galaxy-weighted statistic of DMW to the Las Campanas Redshift Survey. We derive a one-dimensional rms velocity for individual galaxies relative to their neighbors of $\sigma_1 = 126 \pm 10$ km s $^{-1}$ on scales $\sim 1h^{-1}$ Mpc.

Using this new statistic, we find that the observed velocities remain quite cold relative to the predictions of high- Ω_m N -body simulations. Tilting the power spectrum to reduce the initial power on small scales does little to resolve this discrepancy. We have also examined flat and open models with $\Omega_m = 0.3$; these models produce significantly lower dispersions than the high-density models. Combining the LCRS data with the predictions based on halos in the simulations, we measure consistent values $\Omega_m \sim 0.2$ for all models, and we can rule out $\Omega_m = 1$ with a high degree of confidence. Our result suggests that the extremely cold dispersion measured in the vicinity of the Local Group (Schlegel, Davis, & Summers 1994; Governato et al. 1997) might be a local anomaly, as currently popular low-density models can reproduce the observed mean dispersion on $1h^{-1}$ Mpc scales. On the other hand, at slightly larger separations, we find evidence that all of the models may again be too hot relative to the observations.

In the future, it will be extremely useful to apply our statistic to upcoming redshift surveys, such as the Sloan Digital Sky and 2dF surveys, which will contain enough galaxies to compute σ_1 precisely for different sub-samples of the galaxy population. The Deep Extragalactic Probe (DEEP; Davis & Faber 1998) and other surveys at high redshift will also provide a measure of the evolution of σ_1 , which can be used to place additional constraints on cosmological parameters and the bias of the galaxy distribution.

J. E. B. acknowledges support from an NSF graduate fellowship. This work was supported in part by NSF grant AST95-28340. HL acknowledges support provided by NASA through Hubble Fellowship grant #HF-01110.01-98A awarded by the Space Telescope Science Institute, which is operated by the Association of Universities for Research in Astronomy, Inc., for NASA under contract NAS 5-26555. We thank C. Frenk and A. Benson for generously providing data from the Virgo simulations, and we thank R. Sheth and R. Juszkiewicz for helpful discussions. We are also grateful to U. Seljak and M. Zaldarriaga for making their CMBFAST code publicly available, and we thank D. Eisenstein for the HOP code.

REFERENCES

- Baker, J. E., Davis, M., & Ferreira, P. G. 1999, in preparation
- Baker, J. E., Davis, M., Strauss, M. A., Lahav, O., & Santiago, B. X. 1998, *ApJ*, 508, 6
- Bean, A. J., Efstathiou, G., Ellis, R. S., Peterson, B. A., & Shanks, T. 1983, *MNRAS*, 205, 605
- Benson, A. J., Cole, S., Frenk, C. S., Baugh, C. M., & Lacey, C. G. 1999, *MNRAS*, submitted (astro-ph/9903343)
- Brainerd, T. G., Bromley, B. C., Warren, M. S., & Zurek, W. H. 1996, *ApJ*, 464, L103
- Brieu, P. P., Summers, F. J., & Ostriker, J. P. 1995, *ApJ*, 453, 566
- Davis, M., Efstathiou, G., Frenk, C. S., & White, S. D. M. 1985, *ApJ*, 292, 371
- Davis, M. & Faber, S. M. 1998, in *Wide Field Surveys in Cosmology*, ed. S. Colombi, Y. Mellier, & B. Raban (Paris: Editions Frontieres), 333
- Davis, M., Miller, A., & White, S. D. M. 1997, *ApJ*, 490, 63 (DMW)
- Davis, M., Nusser, A., & Willick, J. A. 1996, *ApJ*, 473, 22
- Davis, M. & Peebles, P. J. E. 1983, *ApJ*, 267, 465
- de Lapparent, V., Geller, M. J., & Huchra, J. P. 1988, *ApJ*, 332, 44
- Diaferio, A. & Geller, M. J. 1996, *ApJ*, 467, 19
- Eisenstein, D. J. & Hut, P. 1998, *ApJ*, 498, 137
- Fisher, K. B., Davis, M., Strauss, M. A., Yahil, A., & Huchra, J. P. 1994, *MNRAS*, 267, 927
- Fisher, K. B., Huchra, J. P., Strauss, M. A., Davis, M., Yahil, A., & Schlegel, D. 1995, *ApJS*, 100, 69
- Governato, F., Moore, B., Cen, R., Stadel, J., Lake, G., & Quinn, T. 1997, *New Astronomy*, 2, 91
- Hale-Sutton, D., Fong, R., Metcalfe, N., & Shanks, T. 1989, *MNRAS*, 237, 569
- Jing, Y. P. & Boerner, G. 1998, *ApJ*, 503, 502
- Jing, Y. P., Mo, H. J., & Borner, G. 1998, *ApJ*, 494, 1
- Juszkiewicz, R., Fisher, K. B., & Szapudi, I. 1998, *ApJ*, 504, L1
- Juszkiewicz, R., Springel, V., & Durrer, R. 1999, *ApJ*, 518, L25
- Kepner, J. V., Summers, F. J., & Strauss, M. A. 1997, *New Astronomy*, 2, 165
- Landy, S. D., Szalay, A. S., & Broadhurst, T. J. 1998, *ApJ*, 494, L133
- Marzke, R. O., Geller, M. J., da Costa, L. N., & Huchra, J. P. 1995, *AJ*, 110, 477
- Mo, H. J., Jing, Y. P., & Borner, G. 1993, *MNRAS*, 264, 825
- Okumura, S. K., Makino, J., Ebisuzaki, T., Fukushige, T., Ito, T., Sugimoto, D., Hashimoto, E., Tomida, K., et al. 1993, *PASJ*, 45, 329
- Perlmutter, S., Aldering, G., Goldhaber, G., Knop, R. A., Nugent, P., Castro, P. G., Deustua, S., Fabbro, S., et al. 1999, *ApJ*, 517, 565
- Santiago, B. X., Strauss, M. A., Lahav, O., Davis, M., Dressler, A., & Huchra, J. P. 1995, *ApJ*, 446, 457
- Schlegel, D., Davis, M., & Summers, F. J. 1994, *ApJ*, 427, 527
- Seljak, U. & Zaldarriaga, M. 1996, *ApJ*, 469, 437
- . 1998, CMBFAST
- Shectman, S. A., Landy, S. D., Oemler, A., Tucker, D. L., Lin, H., Kirshner, R. P., & Schechter, P. L. 1996, *ApJ*, 470, 172
- Sheth, R. K. 1996, *MNRAS*, 279, 1310
- Sigad, Y., Eldar, A., Dekel, A., Strauss, M. A., & Yahil, A. 1998, *ApJ*, 495, 516
- Somerville, R. S., Primack, J. R., & Nolthenius, R. 1997, *ApJ*, 479, 606
- Willick, J. A. & Strauss, M. A. 1998, *ApJ*, 507, 64
- Zurek, W. H., Quinn, P. J., Salmon, J. K., & Warren, M. S. 1994, *ApJ*, 431, 559